ADVANCED FUNCTIONAL MATERIALS
www.afm-journal.de

Quaternary Diamond-Like Chalcogenidometalate Networks as Efficient Anode Material in Lithium-Ion Batteries

*Thomas Kaib, Sima Haddadpour, Hanne Flåten Andersen, Leonhard Mayrhofer, Tommi T. Järvi, Michael Moseler, Kai-Christian Möller, and Stefanie Dehnen**

An improvement of lithium-ion batteries with regard to their reversible capacity, cycling stability, rate performance, and safety under repetitive charge and discharge still requires considerable research activity. However, graphite has remained the unexcelled material for the anode so far. Here, it is shown that two novel quaternary lithium-chalcogenidometalate phases, $Li_4MnGe_2S_7$ (1) and $Li_4MnSn_2Se_7$ (2), represent very promising new anode materials for lithium-ion cells in that they achieve specific lithium storage capacities higher than that of the commercially used graphite, and display an excellent stability during cycling. These properties are based on the structural peculiarities of the phases, which adopt Wurtzite-related topologies and provide high structural flexibility of the metal sulfide or selenide bonds as advantageous pre-requisitions for a large ion accessible volume.

1. Introduction

Over the last decades, compounds with high lithium ion uptake capability have attracted attention among solid state and material chemists and physicists, due to their potential application as electrodes in lithium ion secondary batteries. Before 1985, only lithium metal and lithium alloys were used as anode materials. But regarding the safety problems of lithium metal, other substitutes have been extensively investigated. Graphite, with a theoretical capacity of 372 mAh/g, has so far been the standard anode material in commercial lithium batteries.[1]

However, there is still much research activity in improving the reversible capacity, cycling stability, rate performance, and safety under repetitive charge and discharge. For this, several alternative anode materials have been examined.[2–4] A variety of materials—mostly tin or silicon compounds—belong to the most interesting candidates. Especially silicon has shown to be very attractive, due to a very high theoretical capacity of approximately 4000 mAh/g, with a maximum uptake of 4.4 equivalents of Li per Si atom in $Li_{22}Si_5$. The main challenge for the implementation of these composite anodes is the large volume change during lithium insertion and extraction. This amounts to up to 300% which in many cases leads to pulverization of the active particles and poor cycle stability.[4,5] Beside well-known compounds that are capable of lithium intercalation, like TiS_2, MoS_2 or WS_2, for instance,[6–12] a diversity of tin based materials, such as nanostructured carbonaceous matrix compounds or tin composite oxide (TCO) containing Sn(II)O as the active center for lithium, were reported but none of them were superior to the currently used graphite due to their capacity fading.[13–18]

In the course of our studies, we succeeded to synthesize a completely new class of compounds with anionic networks, which show promising capability to lithium ion uptake. Extending our research on chalcogenidotetralates and chalcogenidometalates,[19–21] we are currently focusing on related ternary and quaternary lithium salts of the general type $Li_m[T_xE_z]$ and $Li_m[M_xT_yE_z]$ (T = Ge, Sn; E = S, Se; M = transition metal atom) with Li^+ conduction or storage properties.[22,23] Regarding lithium uptake, compounds with anionic network structure and lithium ions located in the holes of the network seemed to be promising candidates, since (a) the spatial preconditions are advantageous owing to relatively large T–E and M–E distances, and (b) the interaction of the entering hard lithium ions with the soft hosting chalcogenide anions should not be too strong.

Herein we present the first results in the field of lithium-uptaking quaternary chalcogenidometalate networks with the two novel phases $Li_4MnGe_2S_7$ (**1**) and $Li_4MnSn_2Se_7$ (**2**), which indeed combine excellent electrode material properties such as high specific capacity and cycle stability, thus making the networks very interesting as anode materials for lithium-ion batteries.

T. Kaib, Dr. S. Haddadpour, Prof. S. Dehnen
Fachbereich Chemie and Wissenschaftliches Zentrum für Materialwissenschaften (WZMW)
Philipps-Universität Marburg
Hans-Meerwein-Straße, D-35032 Marburg, Germany
E-mail: dehnen@staff.uni-marburg.de
H. F. Andersen
Fraunhofer-Institut für Silicatforschung ISC
Neunerplatz 2, D-97082 Würzburg, Germany
Dr. L. Mayrhofer, Dr. T. T. Järvi, Prof. M. Moseler
Fraunhofer-Institut für Werkstoffmechanik IWM
Wöhlerstraße 11, D-79108 Freiburg, Germany
Dr. K. C. Möller
Fraunhofer-Institut für Chemische Technologie ICT
Joseph-von-Fraunhofer Straße 7, D-76327 Pfinztal, Germany
Dr. T. T. Järvi
Karlsruher Institut für Technologie
Institut für Angewandte Materialien - Zuverlässigkeit von Bauteilen und Systemen IAM-ZBS
Engelbert-Arnold-Straße 4, D-76131 Karlsruhe, Germany

DOI: 10.1002/adfm.201301025

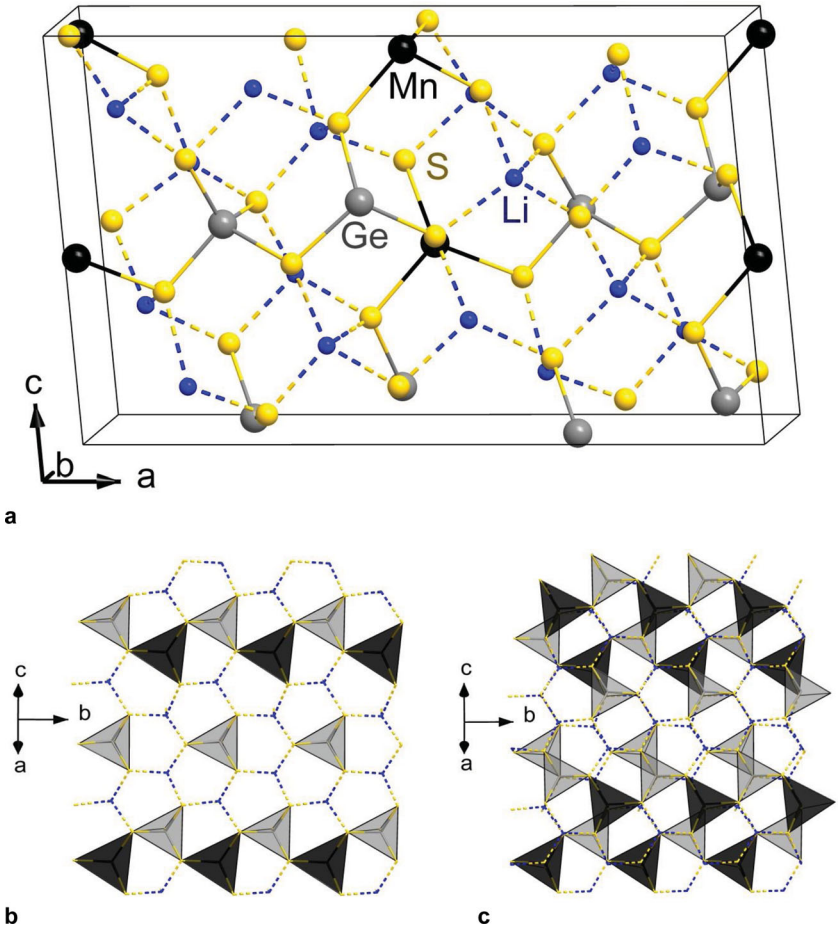

Figure 1. Crystal structure of 1. a) Unit cell of **1** viewed approximately down the b axis. b) View of a layer fragment of the structure of **1** perpendicular to the [102] direction. c) Addition of a second layer to form the 3D network. Color code: Ge, grey; Li, blue; S, yellow; Mn, black.

2. Results and Discussion

2.1. Syntheses and Crystal Structures

$Li_4MnGe_2S_7$ (**1**) and $Li_4MnSn_2Se_7$ (**2**) were obtained by fusion of a stoichiometric amount of Li_2E, Mn, T (= Ge or Sn, respectively) and E (= S or Se, respectively). The compounds are obtained in reasonable yields, but have to be purified by separation from by-products prior to any measurements. Fortunately, the only by-products are either water-soluble ternary Li/T/E salts or elemental chalcogens. The first can be easily extracted with water, thereby not diminishing the yield of the insoluble products; the chalcogens are conveniently removed by sublimation under reduced pressure. The crystal structures of **1** and **2** were determined by means of single-crystal X-ray diffraction, and the phase purity was confirmed by powder X-ray diffraction (see the Supporting Information).

Both compounds crystallize in the monoclinic space group *Cc* (no. 9) with four formula units per unit cell, and both represent three-dimensional (3D) networks with interatomic connectivities analogous to that of the hexagonal diamond topology.[24] Hence, all atoms are four-coordinate, within slightly distorted $[ME_4]$ and $[EM_4]$ *pseudo*-tetrahedra (M = Li, Mn, Ge/Sn; E = S/Se). The unit cells are shown in **Figures 1**a and **Figure 2**a. Naturally, the presence of four different types of atoms leads to a dramatic reduction of the crystallographic symmetry as compared with the hexagonal diamond. In contrast to binary ME derivatives like Wurtzite ZnS with strictly alternating M and E positions, or ternary $MM'E_2$ derivatives like $CuFeS_2$ or $LiAlSe_2$, the number of variants with different regular distributions of the diverse metal atom types among the sites in the structure is naturally much higher.[25–28] Indeed, compounds **1** and **2** exhibit different patterns of their metal atom distributions and thus their crystal structures within the invariant matrix of E atoms that occupy every second atomic site. This is clearly visible by comparing layer sections of the structure perpendicular to the [102] direction. As illustrated in Figure 1b, the respective layer in **1** contains zig-zag chains of corner-linked $[GeS_4]$ and $[MnS_4]$ units along the *b* axis. These are separated from each other by zig-zag chains of $[LiS_4]$ tetrahedra, wich extend in parallel fashion, and by $[GeS_4]$ tetrahedra between the latter. The next layer in the [102] direction is generated through a glide mirror plain symmetry operation (Figure 1c) and gives rise to a 3D network.

In **2**, two $[SnSe_4]$ units and one $[MnSe_4]$ unit form trimeric blocks by corner-sharing of the tetrahedra parallel to [10–2] (Figure 2b). These blocks are separated from each other by a grid of ($[LiS_4]_4$) blocks that also extend along [10–2]. Again, a glide mirror plain adds the next layer in the [102] direction to form the 3D network (Figure 2c).

2.2. Microstructure

Figure 3 shows the SEM images of the new anode materials. A view of the microstructure of $Li_4MnGe_2S_7$ (**1**) and $Li_4MnSn_2Se_7$ (**2**) after pulverization of single crystals is given in Figure 3a,c, respectively, indicating particles in the range of 20–80 μm. Embedding of the particles of **1** and **2** on the as-prepared electrode surfaces (see Methods) is illustrated in Figure 3b,d, respectively. After ball milling the particle size of the active material is reduced, averaging at 2–10 μm. No aggregation of the particles takes place, and the conductive agent is well dispersed between the active material particles. Both samples show similar microstructures, such that different influences of the size and distribution of the particles on the electrochemical behavior are not expected.

2.3. Electrochemical Properties

The cyclic voltammograms of $Li_4MnGe_2S_7$ (**1**) and $Li_4MnSn_2Se_7$ (**2**) with a three-electrode setup, involving lithium metal both

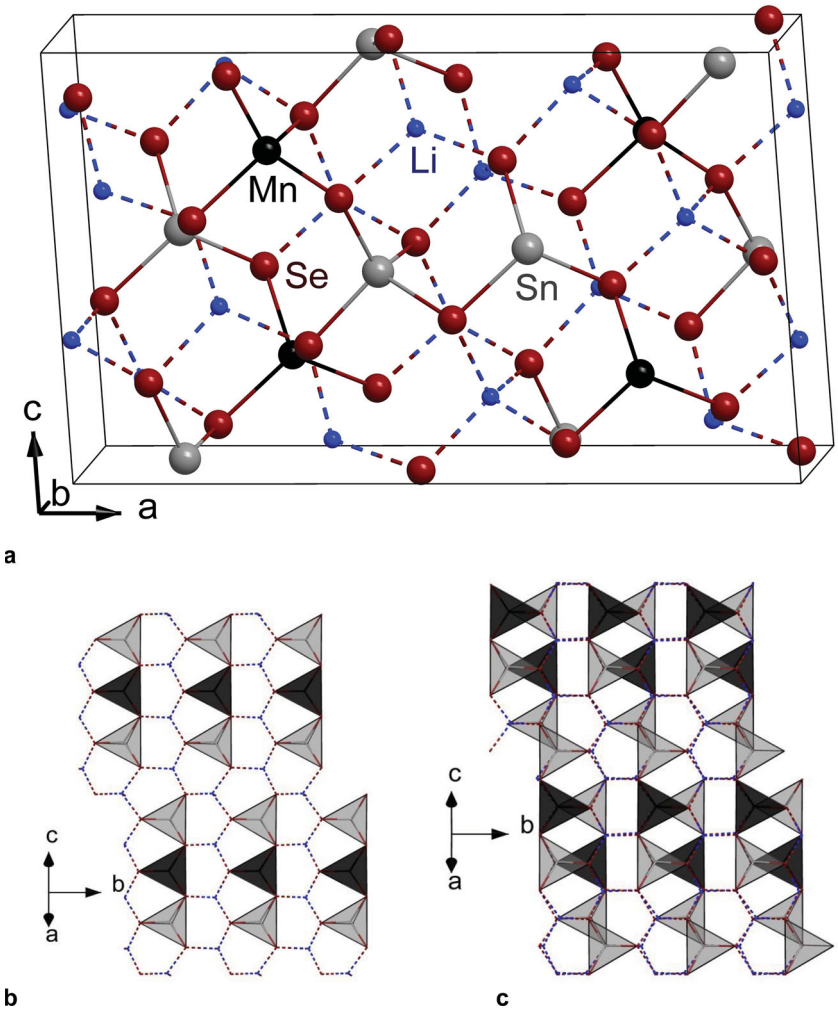

Figure 2. Crystal structure of 2. a) Unit cell of **2** viewed approximately down the b axis. b) View of a layer fragment of the structure of **2** perpendicular to the [102] direction. c) Addition of a second layer to form the 3D network. Color code: Sn, grey; Li, blue; Se, red; Mn, black.

as counter electrode and reference electrode, are given in **Figure 4**. The cyclic voltammogram of **1** (Figure 4a) indicates a significant difference between the first and the following cycles. Several peaks are visible only in the first cycle and represent irreversible reactions. Although the electrochemical activity of **1** is reduced in the next cycle, indicating the compound as being not completely stable, step-wise take-up of Li^+ can be assumed, according to the following reaction for the $x + 1^{st}$ step (Equation 1; $x \geq 0$):

$$Li_{4+x}MnGe_2S_7 + Li^+ + e^- \underset{Discharge}{\overset{Charge}{\rightleftarrows}} \text{“}Li_{4+x+1}MnGe_2S_7\text{”} \quad (1)$$

The cyclic voltammogram of **2** (Figure 4b) shows similar features, including several reduction peaks, which correspond with irreversible reactions, such as solvent decomposition and formation of a passivating film on the electrode surface or structural changes upon the first charge (see also below). Introduction of Li^+ into the material is observed at 1.3 V and between 0.3 and 0.01 V, whereas Li^+ extraction potentials are found at 0.6 V, 1.2 V and 1.7 V. Several peaks that remain stable during cycling indicate a step-wise take-up of lithium ions, similar to the process sketched in Equation 1. Figure 4c shows the two first charge and discharge curves of compound **1**, cycled at a current density of 100 mA/g between 3.0 and 0.01 V. As can be seen, the plateaus in Figure 4c are in accordance with the findings for **1** in the cyclic voltammogram (Figure 4a). Distinct plateaus from the lithiation can be observed in the first cycle at 2.0, 1.6, 1.0 and 0.8 V, whereas the delithiation shows significant plateaus at 1.9 and 2.3 V. **1** obtains an specific delithiation capacity of 1257 mAh/g in the first cycle, which is reduced to 1051 mAh/g after the second cycle. The initial charge and discharge curves of **2** can be seen in Figure 4d. They are also in accordance with the findings of the cyclovoltammogram of **2** (Figure 4b). Lithiation plateaus are found at 1.8, 1.5, 1.3 and 0.7 V, while delithiation is observed at 0.6, 1.2 and 1.7 V. Common for the charge/discharge curves is the slight change in voltage of the plateaus in the second cycle, indicating some irreversible reactions in the first cycle and structure change of the material (see below). Further cycling behavior of compounds **1** and **2** is displayed in **Figure 5** as the discharge capacity and the coulombic efficiency as a function of the cycle number. The capacities after 5 initial cyclovoltammogram cycles are observed at 585 mAh/g (**1**) or 725 mAh/g (**2**), respectively. Despite a small decrease of the maximum discharge capacity of **1**, it still remains at more than 450 mAh/g after 50 cycles. The capacity and its retention are even higher in the case of **2**: the maximum value of 725 mAh/g remains nearly unchanged over the cycles to be 660 after 50 cycles. The coulombic efficiency of compound **1** reaches a value of 96% after the first 20 cycles, whereas for compound **2** a coulombic efficiency of 98% is obtained. The discrepancy between the specific discharge capacities found in the initial cycles (Figure 4) and the in the further cycling behaviour (Figure 5) can be explained through a structural change upon cycling and initial irreversible capacities. However, both materials achieve a stable specific capacity higher than that of the commercially used graphite, thus indicating the promising quality of this new class of potential anode materials based on chalcogenidometalate networks with diamond topology.

2.4. Simulation of the Charging Process

Since the first cycle in the cyclic voltammogram strongly deviates from the subsequent cycles, irreversible changes in the structure of compounds **1** and **2** are likely to occur. Moreover, a simple estimate of the maximal capacity of **2** under the assumption of a pure intercalation process that does not alter

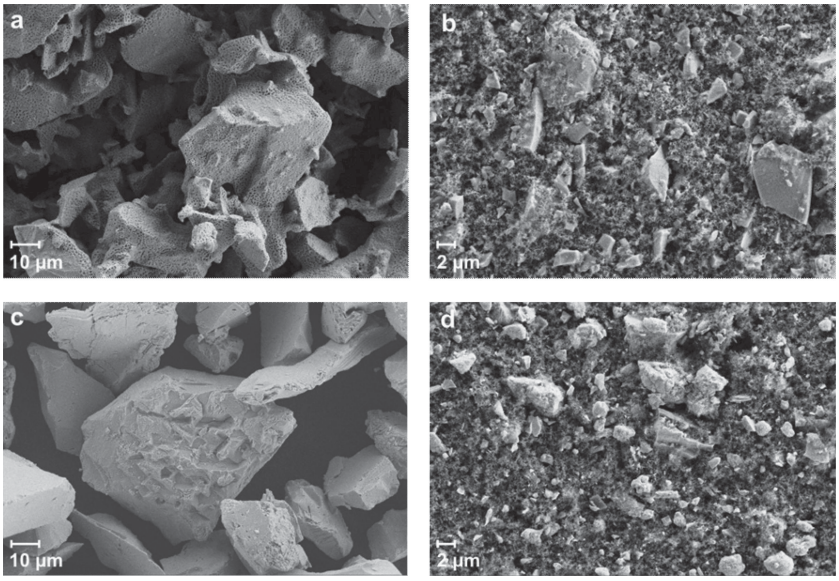

Figure 3. SEM images of the anode materials. a) Pulverized sample of $Li_4MnGe_2S_7$ (**1**). b) As-prepared electrode surface embedding **1**. c) Pulverized sample of $Li_4MnSn_2Se_7$ (**2**). d) As-prepared electrode surface embedding **2**.

the original network of **2** yields a value of only 430 mAh/g, well below the measured maximal capacity of 725 mAh/g. For the estimate, it has been assumed that all 7 tetrahedral and 7 octahedral interstitial sites per formula unit of **2** are each occupied by one lithium ion. In order to resolve the discrepancy between measured and estimated maximal capacities and to investigate the distinct behavior of the first cycle with respect to the subsequent cycles, density functional theory (DFT) within the local spin density approximation has been used to simulate the charging process of material **2** during the first cycle. Starting from the primitive unit cell of **2** with two formula units, the number of lithium ions in the unit cell was successively increased and the binding energies of the additional lithium ions were determined as a function of lithium content. The simulation was carried out until 46 additional lithium ions were incorporated into the original unit cell, corresponding to a capacity of 705 mAh/g. A detailed description of the simulation is given in the Methods section.

Figure 6 shows the binding energy vs. Li^0 of each additional lithium ion as a function of lithium content. Due to the small unit cell in the simulation, the potential is subject to large fluctuations. Hence, the curve was smoothened by averaging over three neighboring values.

The potential curve shows a strong dip at a capacity around 320 mAh/g preceded by a potential plateau ranging from 140 mAh/g to 275 mAh/g. This hints at a structural change of the host material. This picture is supported by comparing the host matrix structure corresponding to lithium contents just

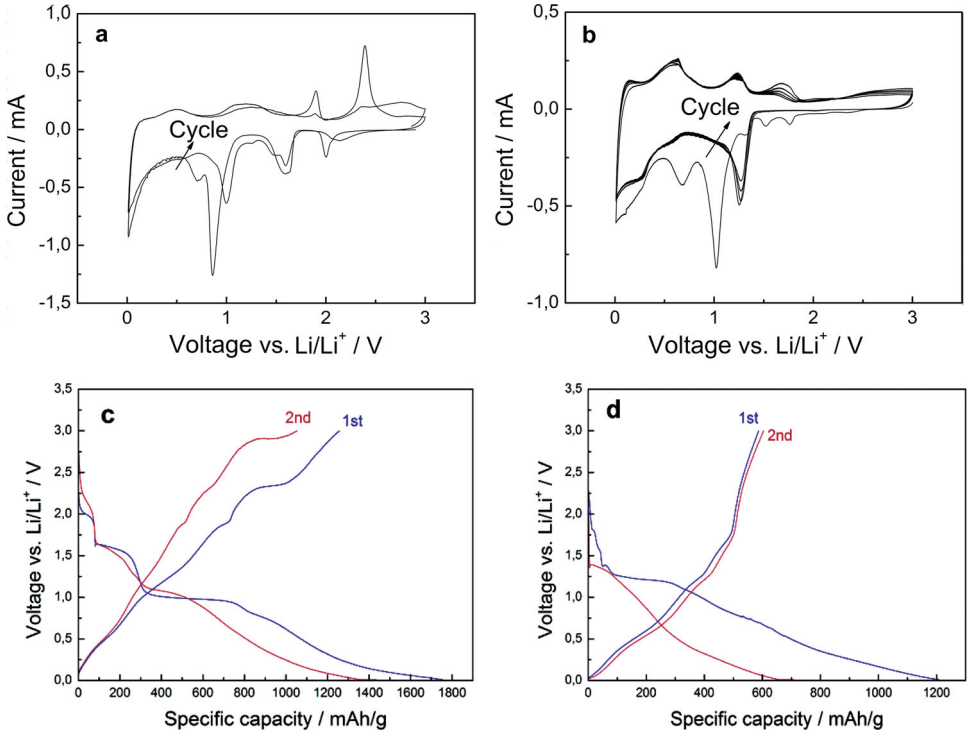

Figure 4. Electrochemical characterizations of the title compounds. Cyclic voltammetry of a) $Li_4MnGe_2S_7$ (**1**) b) $Li_4MnSn_2Se_7$ (**2**). The samples were cycled between 3.0–0.01 V with a scan rate of 0.1 mV/s. The first two charge and discharge curves at a current density of 100 mA/g of c) **1** and d) **2**. The first cycles indicate preliminary, irreversible processes whereas the following cycles show stabilization.

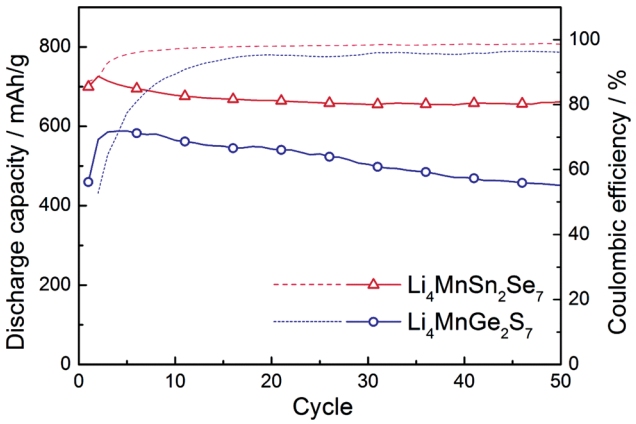

Figure 5. Cyclic behavior of the title compounds. Discharge capacity (solid lines) and coulombic efficiency (dashed lines) as a function of cycle number (after 5 initial cycles with cyclic voltammetry). The cells were cycled between 3.0–0.01 V with a constant current of 100 mA/g.

before, at and beyond the plateau. At 107 mAh/g, the original structure of **2** is still present with the additional lithium ions occupying interstitial positions (except for two lithium ions that have exchanged positions with tin ions). However, after the onset of the plateau, the host matrix starts to deviate more and more from the original structure and finally becomes strongly disordered, as shown in **Figure 7**.

In agreement with the simulation, powder diffraction data of **2** after the first charging cycle did not provide any structural information, thus suggesting the formation of a phase without long-range order. Thus, both simulation and experiment suggest that compound **2** undergoes an irreversible phase change during the first charging process leading to an amorphous, highly cyclable and high capacity phase of **2** observed in the subsequent charge/discharge cycles.

Furthermore, we have analyzed the structural evolution during the first charging by monitoring the coordination of

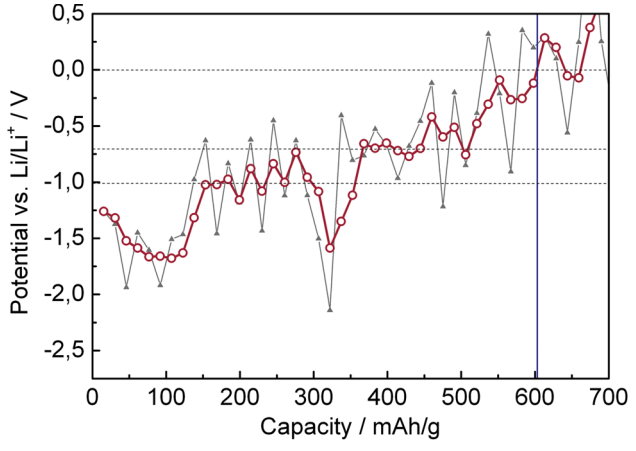

Figure 6. Calculated potential versus capacity of **2**. Triangles show the lithium binding energy vs. Li^0 versus lithium content while circles show a smoothened curve. Horizontal lines indicate the potential of the reduction peaks of the first charging at 1.0 V, 0.7 V and the Li/Li^+ potential respectively. A vertical line indicates the maximal capacity. Lines between simulated data points merely serve as a guide to the eye.

lithium ions by selenium. We find that at the beginning of the charging cycle all lithium ions have at least four selenium neighbors, as expected from a pure intercalation into the network of **2**. However, starting from a lithium content of 150 mAh/g, the fraction of lithium ions with less than four selenium neighbors increases continuously until finally even a lithium fraction evolves that has no direct selenium coordination, see Supporting Information Figure S3. Hence, a pure metal phase forms alongside with a selenium-rich phase.

Since the simulation does not account for any side reactions, a direct comparison between the experimental and simulated potential curves of the first charging cycle is not feasible. However, because it excludes the side reactions, it can be used as a model to explain the observed discharge capacity of the material. Indeed, the capacity obtained from the simulation has a value of 600 mAh/g, matching the capacity after 50 cycles in Figure 3c well. The slightly lower value from the simulation is likely explained by the fact that the simulation does not necessarily find the global energy minimum, slightly shifting the curve in Figure 6 upwards.

3. Conclusions

Two novel chalcogenidometalate networks, $Li_4MnGe_2S_7$ (**1**) and $Li_4MnSn_2Se_7$ (**2**), were synthesized by application of polychalcogenide flux techniques as phase pure single-crystalline products. Both compounds show promising electrochemical properties for application as anode materials in lithium ion batteries. The specific capacities of 585 mAh/g (**1**) and 725 mAh/g (**2**), exceed the value of the commercially used graphite with a theoretical capacity of 372 mAh/g. In addition, compounds **1** and **2** show an excellent cycling stability with more than 450 mAh/g after 50 cycles for **1** and 660 mAh/g after 50 cycles for **2**. DFT simulations were in the position to describe the charging/de-charging processes, thereby identifying an irreversible phase change during the first charging process, which leads to the highly cyclable, high capacity, amorphous phase.

4. Experimental Section

General: All reaction steps were performed with strong exclusion of air and external moisture under Ar atmosphere at a high-vacuum, double-manifold Schlenk line or N_2 atmosphere in a glove box (MBraun). Elements were purchased from Sigma-Aldrich (Sn, Li) and Riedel de Haën (Se) and used without further purification. Li_2S and Li_2Se were prepared according to literature procedures.[29] Water was degassed by applying dynamic vacuum (10^{-6} Pa) for several hours.

*Synthesis of $Li_4MnGe_2S_7$ (**1**)/ $Li_4MnSn_2Se_7$ (**2**)*: A stoichiometric mixture of Li_2S (0.706 g, 15.36 mmol) or Li_2Se (0.686 g, 15.36 mmol), Ge (1.114 g, 15.36 mmol) or Sn (0.877 g (7.39 mmol), S (1.969 g, 61.41 mmol) or Se (2.335 g, 29.57 mmol), and Mn (0.211 g, 3.84 mmol or 0.102 g, 1.85 mmol), respectively, was melted together in a furnace with a definite temperature program: heating up to 650 °C, with a heating rate of 18 °C/h, keeping for 24 h at 650 °C, cooling down to room temperature, with a rate of 6 °C/h. The product was obtained as single-crystalline phase beside diverse ternary Li/Ge/S (Li/Sn/Se) phases like Li_4GeS_4 (Li_4SnSe_4) and excess of sulfur (selenium).[30] To obtain the phase-pure product, the mixture was washed with water to remove the soluble by-products, and the surplus of sulfur or selenium

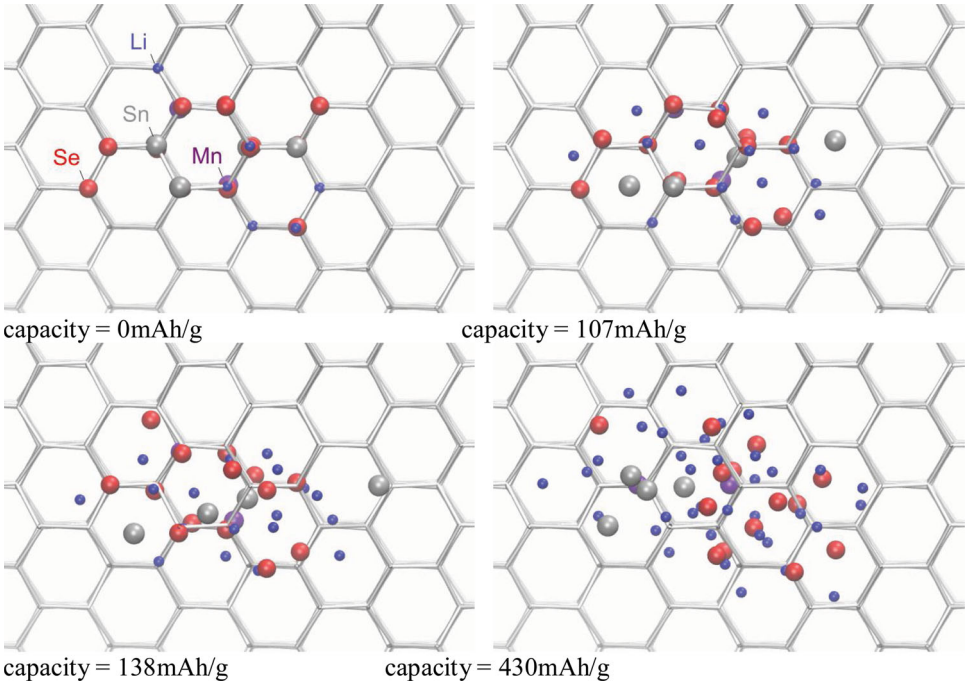

Figure 7. Calculated structural evolution of **2** during first charging. The figures show the atoms within the irreducible unit cell of **2** for different lithium contents. The original diamond structure of uncharged **2** is displayed as a wire model for comparison.

was removed via sublimation at 320 °C (500 °C) and reduced pressure of ≈10^{-6} Pa. Yield: 1.653 g (3.66 mmol, 95.2% based on Mn) for **1** and 1.497 g (1.715 mmol, 92.7% based on Mn) for **2**.

X-Ray Structural Analyses: Single-crystal X-ray diffraction data were collected on a diffractometer equipped with a STOE imaging plate detector system IPDS2T, using graphite-monochromized Mo-K_α radiation ($\lambda = 0.71073$ Å) at $T = 100$ K. Structure solution and refinement were performed by direct methods and full-matrix least-squares on F^2, respectively, using ShelxTL software.[31–33] Crystal data for $Li_4MnGe_2S_7$ (**1**): 452.3 g·mol^{-1}, monoclinic, space group *Cc*, light pink block crystal, $0.13 \times 0.12 \times 0.08$ mm^3, $a = 16.833(3)$ Å, $b = 6.7092(13)$ Å, $c = 10.121(2)$ Å, $\beta = 94.76(3)°$, $V = 1139.1(4)$ Å^3, $Z = 4$, ρ(calc.) = 2.637 g·cm^{-3}, 2θ = 5–51°, 2835 reflections collected, 1817 independent reflections [$R_{int} = 0.1601$], 1638 with $I > 2\theta(I)$; $\mu(Mo_{K\alpha}) = 7.555$, *GOF* = 1.100, $R_1 = 0.0561$, $wR_2 = 0.1773$ for $I > 2\sigma(I)$. Crystal data for $Li_4MnSn_2Se_7$ (**2**): 872.8 g·mol^{-1}, monoclinic, space group *Cc*, orange block crystal, $0.20 \times 0.16 \times 0.09$ mm^3, $a = 18.126(4)$ Å, $b = 7.2209(14)$ Å, $c = 10.740(2)$ Å, $\beta = 93.43(3)$ °, $V = 1403.2(5)$ Å^3, $Z = 4$, ρ(calc.) = 4.132 g·cm^{-3}, $2\theta = 5–53°$, 5620 reflections collected, 2881 independent reflections [R_{int} = 0.0942], 2740 with $I > 2\theta(I)$; $\mu(Mo_{K\alpha}) = 22.526$, *GOF* = 1.088, R_1 = 0.0466, $wR_2 = 0.1277$ for $I > 2\sigma(I)$. Further details of the crystal structure investigation(s) may be obtained from the Fachinformationszentrum Karlsruhe, D-76344 Eggenstein-Leopoldshafen (Germany), on quoting the depository numbers CSD-425763 and -425764. For additional information and details of the refinement, see the Supporting Information.

Electrochemical Properties: Cyclic voltammograms and cycle behavior curves were measured with three-electrode Swagelok-type cells where lithium metal was used as both counter electrode and reference electrode. The electrolyte used was a 1 M $LiClO_4$ in a 1:1 mixture of ethylene carbonate (EC) and ethylmethyl carbonate (EMC). One layer Celgard 2325 as well as one layer Freudenberg FS2019 were used as cell separators. Both $Li_4MnSn_2Se_7$ and $Li_4MnGe_2S_7$ were prepared as composite electrodes of anode material (60%), carbon black (28%) and polyvinylidene fluoride (PVDF) binder (12%), homogeneously mixed in *N*-methyl pyrrolidone (NMP) solvent. The components were mixed in a planetary micro mill (Fritsch) and coated uniformly on a copper foil. After drying at room temperature in a glove box (MBraun) under argon atmosphere, the electrodes were punched into a wanted disk shape and further dried under vacuum at 80 °C for 5 h. The assembly of the cells was conducted under argon-filled atmosphere. The cyclic voltammetry was performed with a potentiostat (Solartron CellTest® System 1470) and the scans were recorded from 3.0 to 0.01 V with a scan rate of 0.1 mV/s. The measurements recording the cyclic behavior were performed on a Maccor 4000 battery tester, the cells cycled between 3.0 to 0.01 V at room temperature with a current density of 100 mA/g.

Simulations: The first charging cycle of **2** was simulated within the DFT framework. The starting point of the charging simulation was the primitive unit cell of **2** with two formula units. Using the Monte Carlo algorithm described in the Supporting Information, the interstitial sites of the initial structure were filled with additional lithium ions and all configurations with a single additional lithium ion were extracted. The different configurations were then relaxed using the SIESTA DFT code.[34] From the relaxed configurations the one with the lowest energy was chosen. For this minimal energy configuration, again, all interstitial sites were occupied by lithium and the resulting configurations now with two additional lithium ions were relaxed and the corresponding new minimal energy configuration was determined. This was then continued until inserting more lithium no longer was favorable in energy. The obtained minimal energy configurations for each lithium content were further relaxed using the Vienna ab initio simulation package (VASP) (see Ref. [35] and references therein) to obtain basis set independent high-accuracy results. Thereby some of the structures still relaxed considerably. The detailed parameters of the DFT calculations are given below.

DFT Parameters SIESTA: Exchange and correlation are described within the spin-polarized local density approximation (LSDA).[36] The effects of the core electrons are taken into account by the use of norm-conserving pseudo-potentials.[37–39] A double zeta plus polarization (DZP) basis is employed for the wavefunction expansion.[40] The radial cutoff of the basis orbitals is determined by an energy shift of 0.02 Ry in the radial part of the pseudo-atom Schrödinger equation.[34] The spacing

of the real-space integration grid is determined by a mesh cutoff energy of 100 Ry. Forces have been relaxed to values smaller than 0.04 eV/Å.

DFT Parameters VASP: LSDA calculations with the PAW method and pseudopotentials were performed with the "Accurate" presets in VASP 5.2 and with a plane-wave cutoff of 351 eV.[41,42]

For both DFT packages, the Monkhorst-Pack scheme was used to sample the Brillouin-zone using 4 k-points in each direction.[43] For SIESTA and VASP we used Fermi-Dirac and Gaussian smearing, respectively, with a width of 0.1 eV.

Supporting Information

Supporting Information is available from the Wiley Online Library or from the author.

Acknowledgements

This work was supported by the Deutsche Forschungsgemeinschaft (DFG) and the Bundesministerium für Bildung und Forschung (BMBF, project "KoLiWIn"/03SF0343G and 03SF0343D). T. J. acknowledges funding from the Academy of Finland (project no. 136165).

Received: March 24, 2013
Revised: May 2, 2013
Published online: June 20, 2013

[1] W. J. Zhang, *J. Power Sources* **2011**, *196*, 13.
[2] H. Li, Z. Wang, L. Chen, X. Huang, *Adv. Mater.* **2009**, *21*, 4593.
[3] L. Ji, Z. Lin, M. Alcoutlabi, X. Zhang, *Energy Environ. Sci.* **2011**, *4*, 2682.
[4] D. Deng, M. G. Kim, J. Y. Lee, J. Cho, *Energy Environ. Sci.* **2009**, *2*, 818.
[5] M. Winter, J. O. Besenhard, *Electrochim. Acta* **1999**, *45*, 31.
[6] N. I. Schwarzburger, R. Knobel, H. Behrens, M. Binnewies, I. Horn, A. Pelster, H. F. Arlinghaus, L. Dörrer, H. Schmidt, *Z. Phys. Chem.* **2012**, *226*, 461.
[7] K. Chang, W. Chen, *Chem. Commun.* **2011**, *47*, 4252.
[8] J. Xiao, D. Choi, L. Cosimbescu, P. Koech, J. Liu, J. P. Lemmon, *Chem. Mater.* **2010**, *22*, 4522.
[9] C. Feng, L. Huang, Z. Guo, H. Liu, *Electrochem. Commun.* **2007**, *9*, 119.
[10] R. A. Gordon, D. Yang, E. D. Crozier, D. T. Jiang, R. F. Frindt, *Phys. Rev. B* **2002**, *65*, 125407–1.
[11] B. K. Miremadi, S. R. Morrison, *J. Appl. Phys.* **1988**, *63*, 4970.
[12] M. A. Gee, R. F. Frindt, P. Joensen, S. R. Morrison, *Mat. Res. Bull.* **1986**, *21*, 543.
[13] J. Fan, T. Wang, C. Yu, B. Tu, Z. Jiang, D. Zhao, *Adv. Mater.* **2004**, *16*, 1432.
[14] M. Noh, Y. Kwon, H. Lee, J. Cho, Y. Kim, M. G. Kim, *Chem. Mater.* **2005**, *17*, 1926.
[15] Y. Wang, F. Su, J. Y. Lee, X. S. Zhao, *Chem. Mater.* **2006**, *18*, 1347.
[16] K. T. Lee, Y. S. Jung, S. M. Oh, *J. Am. Chem. Soc.* **2003**, *125*, 5652.
[17] H. Qiao, Z. Zheng, Z. Zhang, *J. Mater. Sci.* **2008**, *43*, 2778.
[18] Y. Idota, T. Kubota, A. Matsufuji, Y. Maekawa, T. Miyasaka, *Science* **1997**, *276*, 1395.
[19] S. Dehnen, M. Melullis, *Coord. Chem. Rev.* **2007**, *251*, 1259.
[20] S. Haddadpour, M. Melullis, H. Staesche, C. R. Mariappan, B. Roling, R. Clérac, S. Dehnen, *Inorg. Chem.* **2009**, *48*, 1689.
[21] G. Thiele, S. Peter, M. C. Schwarzer, E. Ruzin, R. Clérac, H. Staesche, C. Rößer, B. Roling, S. Dehnen, *Inorg. Chem.* **2012**, *51*, 3349.
[22] T. Kaib, M. Kapitein, S. Dehnen, Z. Anorg, *Allg. Chem.* **2011**, *637*, 1683.
[23] T. Kaib, S. Haddadpour, M. Kapitein, P. Bron, C. Schröder, H. Eckert, B. Roling, S. Dehnen, *Chem. Mater.* **2012**, *24*, 2211.
[24] F. P. Bundy, J. S. Kasper, *J. Chem. Phys.* **1967**, *46*, 3437.
[25] G. Aminoff, *Z. Kristallogr., Kristallgeom., Kristallphys., Kristallchem.* **1923**, *58*, 203.
[26] C. L. Burdick, J. H. Ellis, *J. Am. Chem. Soc.* **1917**, *39*, 2519.
[27] S. R. Hall, J. M. Stewart, *Acta Cryst.* **1973**, *B29*, 579.
[28] J. Kim, T. Hughbanks, *Inorg. Chem.* **2000**, *39*, 3092.
[29] E. A. Axtell, J. H. Liao, M. G. Kanatzidis, *Inorg. Chem.* **1998**, *37*, 5583.
[30] Y. Matsushita, M. G. Kanatzidis, *Z. Naturforsch.* **1998**, *53B*, 23.
[31] G. W. Sheldrick, *Crystal structure solution and refinement software package* SHELXTL 5.1; Bruker AXS Inc.: Madison, WI, **1997**.
[32] *International Tables for Crystallography, Space-Group Symmetry* (Ed: T. Hahn), vol. A, Kluwer Academic Publishers, Dordrecht **1989**.
[33] Absorption correction was applied with the programs X-RED and X-SHAPE included in X-Area 1.43, STOE & Cie GmbH, Hilpertstraße 10, D-64295, Darmstadt. IPSD IIT: Stoe & Cie, X-AREA (Version 1.54) and X-RED32 (Version 1.54), Stoe & Cie, Darmstadt, Germany **2002**.
[34] J. M. Soler, E. Artacho, J. D. Gale, A. García, J. Junquera, P. Ordejón D. Sánchez-Portal, *J. Phys.: Condens. Matter* **2002**, *14*, 2745.
[35] G. Kresse, J. Fürthmüller, *Phys. Rev.* **1996**, *B54*, 11169.
[36] J. P. Perdew, A. Zunger, *Phys. Rev.* **1981**, *B23*, 5048.
[37] D. R. Hamann, M. Schlüter, C. Chiang, *Phys. Rev. Lett.* **1979**, *43*, 1494.
[38] G. B. Bachelet, D. R. Hamann, M. Schlüter, *Phys. Rev.* **1982**, *B26*, 4199.
[39] L. Kleinman, D. M. Bylander, *Phys. Rev. Lett.* **1982**, *48*, 1425.
[40] E. Artacho, D. Sanchez-Portal, P. Ordejon, A. Garcia, J. M. Soler, *Phys. Status Solidi B* **1999**, *215*, 809.
[41] P. E. Blöchl, *Phys. Rev.* **1994**, *B50*, 17953.
[42] G. Kresse, D. Joubert, *Phys. Rev.* **1999**, *B59*, 1758.
[43] H. J. Monkhorst, J. D. Pack, *Phys. Rev.* **1979**, *B13*, 5188.